Elastocapillarity-driven surface growth in tumour spheroids

D. Riccobelli*

MOX – Dipartimento di Matematica, Politecnico di Milano, Piazza Leonardo da Vinci 32, 20133, Milano, Italy

Abstract

Growing experimental evidence highlights the relevant role of mechanics in the physiology of solid tumours, even in their early stages. While most of the mathematical models describe tumour growth as a volumetric increase of mass in the bulk, in vitro *experiments on tumour spheroids have demonstrated that cell proliferation occurs in a thin layer at the boundary of the cellular aggregate. In this work, we investigate how elasticity and surface tension interact during the development of tumour spheroids. We model the tumour as a hyperelastic material undergoing boundary accretion, where the newly created cells are deformed by the action of surface tension. This growth leads to a frustrated reference configuration, resulting in the appearance of residual stress. Our theoretical framework is validated through experimental results of tumour spheroid cutting. Similar to fully developed tumours, spheroids tend to open when subject to radial cuts. Remarkably, even newly formed spheroids, which lack residual stress, exhibit this behaviour. Through both analytical solutions and numerical simulations, we show that this phenomenon is driven by elastocapillary interactions, where the residual stress developed in grown spheroids amplifies the tumour opening. Our model's outcomes align with experimental observations and allow us to estimate the surface tension acting on tumour spheroids.*

1 Introduction

Uncontrolled cell proliferation is the main feature that distinguishes healthy tissues from tumours: while the physiological growth of tissue is tightly regulated and self-limited by cell signalling, tumour cells replicate in an unregulated manner. The huge social impact of cancer has given the impulse to extensive research focused on understanding the mechanisms underlying tumour growth.

Cancer research frequently relies on surrogates to investigate the dynamics of tumour growth, ranging from experiments performed *in vivo* to *in vitro*. In the first type of experiments, tumours are implanted and grown in animals, such as mice [1]. Conversely, *in vitro* experiments involve the cultivation of tumour cells outside a living organism in the laboratory [2]. A notable example is multicellular tumour spheroids, which are three-dimensional structures that self-assemble, forming spherical aggregates.

Tumour spheroids serve as an artificial model mimicking the early stages of tumour development. At this stage, the cells within the spheroid rely on passive intercellular diffusion for the supply of nutrients and oxygen, as blood vessels have not yet penetrated the tumour mass.

Research on tumour spheroids has revealed a strong connection between mechanical forces and tumour proliferation [3]: applying compressive load at the boundary reduces cell mitosis and can induce apoptosis [4–10]. Furthermore, mechanical pressure has been linked to increased invasiveness in cancer cells [11].

In order to understand how boundary loads drive the inner mechanical state, a rheological description of spheroids is essential. Increasing evidence suggests that spheroids exhibit viscoelastic behaviour [8]. For example, similarly to fully developed tumours, spheroids tend to open when subjected to a radial cut [12–14]. If the spheroid obeyed a fluid-like behaviour governed by surface tension, it would reorganize to minimize surface area, returning to a spherical shape. Conversely, radially cut tumour spheroids display a heart-like shape, see Fig. 1. Moreover, even intact tumour spheroids can exhibit both spherical and cylindrical shapes depending on the initial number of cells [13], suggesting that while surface tension plays a role in spheroid physics, other forces also influence its shape.

The mechanical origin of the deformation following the cut is a matter of debate. In [12, 13], the authors argue that the spheroid opening is driven by non-homogeneous volumetric growth within the tumour. In biological systems, non-homogeneous growth can lead to geometrical incompatibilities that generate mechanical stress, known as *residual stress* [16], even in the absence of external load. Volumetric growth and residual stresses have been extensively studied in recent years [7–9], leading to mathematical models that explain a variety of phenomena in biological matter. This has given rise to a field of research known as *morphoelasticity* [8, 17, 18]. Successful applications of morphoelasticity include modelling organ and tissue morphogenesis [19–22], understand-

---
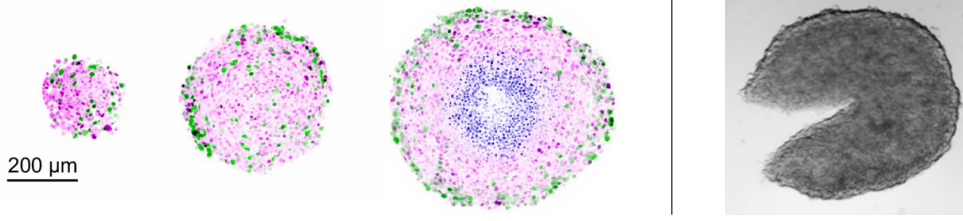
*email: davide.riccobelli@polimi.it

Figure 1: *(Left) Sections of tumour spheroids with varying radii. Recently dividing cells are coloured green, while dying cells are indicated in blue (adapted from [15]). (Right) An incised tumour spheroid two days post-seeding, with an initial cell count of 5000 (adapted from [13]).*

ing deformations in arteries [23, 24], and explaining mechanical instabilities in tumour vessels [25–27].

However, several aspects remain obscure. For instance, the residual stress responsible for tumour opening following a radial cut is peculiar, requiring tensile hoop residual stress in the outer region of the spheroid [3, 8]. Such a stress state can be produced only if cell proliferation decreases near the free surface [28]. The situation in reality is the opposite: even in the early stages of spheroid development, cell mitosis occurs in a narrow region close to the spheroid boundary [5, 6, 15, 29], see Fig. 1. Moreover, the self-aggregation process of tumour cells leading to the formation of tumour spheroids usually takes around two days. In this timeframe, no residual stress should have formed, and thus no opening would be expected when a spheroid is cut. However, Guillaume et al. [13] observed spheroid openings even in these early stages.

During the initial days, only a thin outer layer of cells experiences circumferential tension, while the core remains in an isotropic stress state [30]. This tensional "skin" at the spheroid's boundary can be understood as an effect of tissue surface tension on the cell aggregate generated by intercellular cohesion forces and active contractility, as discussed in [31]. This surface phenomenon primarily arises from intercellular cohesion forces and has been shown to significantly influence the mechanical behaviour of cell aggregates [31, 32], particularly at small scales such as those of a spheroid [14, 33].

The aim of this work is to construct a mathematical model of tumour spheroid growth able to explain the tumour opening following a radial cut. In Section 2, we propose the mathematical model of the spheroid, where tumour proliferation is described as a surface accretion mediated by surface tension. The study of spheroid incision is performed in Section 3, where we propose both a simplified analytical prediction of tumour opening and a quantitative analysis through numerical simulations and comparison with experimental results. Finally, the main results are summarized in Section 4, together with some concluding remarks.

2 Modelling of the elastocapillarity of tumour spheroids

In this section we construct a mathematical model of a tumour spheroid as an elastic body subject to surface tension. First, we describe the mathematical setting in the absence of cell proliferation. Second, we extend the theoretical framework to include surface growth mediated by capillarity effects.

2.1 A continuum model of tumour spheroid with tissue surface tension

The tumour spheroid is treated as an elastic continuum body subject to surface tension. By following the theory of continuum mechanics, we introduce the reference configuration $\Omega_0 \subset \mathbb{R}^3$. Let (e_X, e_Y, e_Z) be the canonical vector basis.

Let $\varphi : \Omega_0 \to \mathbb{R}^3$ be the deformation field, we denote by $\mathbf{F} = \text{Grad}\,\varphi$ the deformation gradient. The current configuration of the body is identified by Ω, i.e. $\Omega = \varphi(\Omega_0)$.

Given a point $X \in \Omega_0$, we denote by x the corresponding point in the current configuration, so that $x = \varphi(X)$. We can introduce the displacement field u as the vector function $u(X) = \varphi(X) - X$.

In order to take into account the large elastic deformations of the tumour, we assume that the cellular aggregate can be described as a hyperelastic material. Let $\psi_r = \psi_r(\mathbf{F})$ be its strain energy density. The *bulk elastic energy* of the body is thus given by

$$\mathcal{E}_{\text{el}}[\varphi] = \int_{\Omega_0} \psi_r(\mathbf{F}) \, \mathrm{d}V. \tag{1}$$

We can also introduce a *surface energy* that models the action of tissue surface tension. As commonly done in the context of cellular aggregate, we take it as directly proportional with the current area a of the external boundary σ_γ, i.e.

$$\mathcal{E}_{\text{s}}[\varphi] = \gamma a = \gamma \int_{\Sigma_\gamma} (\det \mathbf{F}) \, |\mathbf{F}^{-T} N| \mathrm{d}A, \tag{2}$$

where γ is the surface tension, N is the external normal in the reference configuration, Σ_γ is the referential counterpart of the external boundary σ_γ, i.e.

$\sigma_\gamma = \boldsymbol{\varphi}(\Sigma_\gamma)$. The deformation $\boldsymbol{\varphi}$ must minimize the energy of the system $\mathcal{E}$, given by

$$\mathcal{E}[\boldsymbol{\varphi}] = \mathcal{E}_{\text{el}}[\boldsymbol{\varphi}] + \mathcal{E}_{\text{s}}[\boldsymbol{\varphi}]. \tag{3}$$

Since cellular aggregates are mainly composed of water, we can approximate their behaviour as incompressible, namely the deformation must obey the constraint

$$\det \mathbf{F} = 1. \tag{4}$$

The stress can be measured in the reference configuration by means of the first Piola–Kirchhoff stress tensor, given by

$$\mathbf{S} = \frac{\partial \psi_r}{\partial \mathbf{F}} - p\mathbf{F}^{-T}, \tag{5}$$

where p is a scalar field that imposes the incompressibility constraint.

The balance equations corresponding to the minimization of the energy functional (3) are given by

$$\begin{cases} \text{Div } \mathbf{S} = \mathbf{0} & \text{in } \Omega_0, \\ \mathbf{S}\boldsymbol{N} = \gamma \mathcal{K} \mathbf{F}^{-T} \boldsymbol{N} & \text{on } \Sigma_\gamma, \end{cases} \tag{6}$$

where $\mathcal{K}$ is twice the mean curvature of the current surface σ_γ. Rigid body motions can be filtered out, for example, by fixing the displacement of a point of the body and by requiring zero mean rotation.

In order to proceed with the analysis, we have to make some constitutive choice on the mechanical behaviour of the spheroid. In the following, we assume that the body Ω_0 is composed of a neo–Hookean material, so that the strain energy density reads

$$\psi_r(\mathbf{F}) = \frac{\mu}{2} \mathbf{F} : \mathbf{F}, \tag{7}$$

where μ is the shear modulus, while : denotes the Frobenius scalar product of tensors, i.e. $\mathbf{A} : \mathbf{B} = \text{tr } \mathbf{A}^T\mathbf{B}$.

2.2 Surface accretion and surface tension

While the model proposed in the previous section can describe the pure elastic behaviour of a spheroid, it is insufficient to capture what occurs as the spheroid grows. Indeed, spheroids left to grow for several days in an environment with large availability of nutrients can generate mechanical stress as a consequence of their growth. The increase in the opening length of cut spheroids grown for a few days [13] suggests that the growing process enhances the natural opening induced by surface tension by generating a tensile hoop stress in the outer part of the spheroid.

Analogously to spheroids, incised real tumours open up, even though surface tension is negligible due to their larger radius [1]. This deformation results from the release of the tensile hoop stress in the

outer region, while there is a compressive radial residual stress in the core [8]. Puzzlingly, to reproduce this stress pattern using classical volumetric growth theory, the growth of the tumour spheroid should be greater in the inner part rather than the outer part [8, 28], which is precisely the opposite of what is observed in spheroids. In [15], the proliferation of cells in tumour spheroids seems to be mainly concentrated at the periphery within a layer a few cells thick, while cells in the bulk duplicate only rarely, see Fig. 1. Similar behaviours have been reported in [5, 6, 29].

Differently from previous models [7–10, 28], here we describe spheroid's growth as a surface accretion, where new mass is added at the boundary rather than in the bulk. We start by considering a time-dependant reference configuration, i.e. $\Omega_0(t)$. Let R_t be the radius of the (intact) tumour spheroid at time t, so that

$$\Omega_0(t) = \{\boldsymbol{X} \in \mathbb{R}^3 \mid \|\boldsymbol{X}\| < R_t\}.$$

We indicate with $\boldsymbol{\varphi}_t$ the deformation field at time t, so that $\Omega(t) = \boldsymbol{\varphi}_t(\Omega_0(t))$ is the current configuration at a given instant of time. We denote by (R, Θ, Φ) and (r, θ, ϕ) the spherical coordinates in the reference and current configurations, respectively. Similarly, let $(\boldsymbol{e}_R, \boldsymbol{e}_\Theta, \boldsymbol{e}_\Phi)$ and $(\boldsymbol{e}_r, \boldsymbol{e}_\theta, \boldsymbol{e}_\phi)$ the corresponding vector basis.

As the spheroid grows, new particles are added to the system at the boundary of the domain. Due to the presence of surface tension, the spheroid is subject to a mechanical load at the boundary. From (6), we get

$$\mathbf{T}(\boldsymbol{x}, \mathbf{F})\boldsymbol{n} = \gamma \mathcal{K} \boldsymbol{n}, \tag{8}$$

where $\mathbf{T} = \mathbf{S}\mathbf{F}^T$ is the Cauchy stress tensor. As the process of growth is much slower than the characteristic timescale of the deformation, we can safely neglect inertia and the balance equation (6) still holds, with Σ_γ corresponding to the whole boundary $\partial\Omega_0(t)$.

Among the several frameworks proposed to model surface growth, see for instance [34–38], we follow the theory proposed by Truskinovsky and Zurlo in a series of works [39–41]. This approach accounts for the elastic distortions induced by the boundary condition (8) in the material generated on the surface.

To model the elastic frustration in the spheroid, we assume that ψ_r, introduced in (7), represents the strain energy density of the spheroid in its relaxed state for a volume element of mass density ρ_0. We call this function *material archetype* [42]. Specifically, during the deposition of a new particle $\boldsymbol{X}_t$ belonging to the boundary of $\Omega_0(t)$, the material is elastically distorted and the strain energy density in the refer-
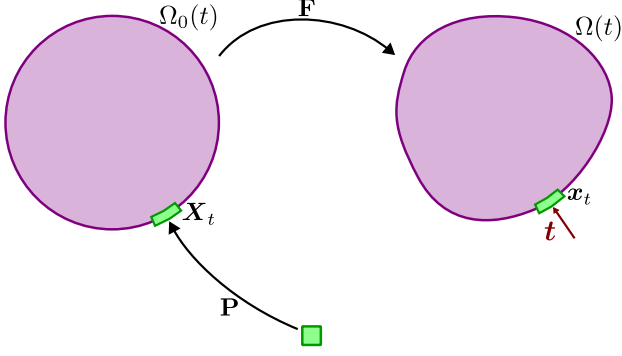
Figure 2: *Representation of the material transplant of a point particle X_t [42]. When a new point is placed at the boundary of the spheroid, it is first subject to an elastic distortion $\mathbf{P}$ from the relaxed state to satisfy the boundary condition $\mathbf{T}n = t$ after the deformation $\mathbf{F}$ is applied.*

ence configuration can be written as

$$\psi(\mathbf{X}_t, \mathbf{F}) = \frac{1}{\det \mathbf{P}(\mathbf{X}_t)} \psi_r(\mathbf{F}\mathbf{P}(\mathbf{X}_t)).$$

We refer to $\mathbf{P}$ as the transplant map, or more simply as *transplant*. Such a tensor models the local elastic distortion from the relaxed archetype to the reference configuration at point X_t, see Fig. 2.

While being on the boundary at time t, the point X_t belongs to the bulk of $\Omega_0(\bar{t})$ for $\bar{t} > t$. Once the material is deposed, here we assume that $\mathbf{P}$ does not change in time. The transplant $\mathbf{P}$ can be also extended to the initial reference configuration $\Omega_0(0)$ by taking $\mathbf{P}(X) = \mathbf{I}$ for $X \in \Omega_0(0)$. In this way, $\mathbf{P}$ is defined in the whole the reference domain for all t, and the energy functional becomes

$$\mathcal{E}_{\mathrm{el}}[\boldsymbol{\varphi}] = \int_{\Omega_0} \psi(\mathbf{X}, \mathbf{F}) \, dV.$$

Such an operation is called *material transplant*. Generally speaking, the reference configuration may not be stress-free if the transplant map $\mathbf{P}(X)$ is not a gradient of a deformation function $\boldsymbol{\varphi}_{\mathbf{P}}(X)$, for a detailed discussion see [18, 42]. In the following, the explicit dependence of $\mathbf{P}$ on the point is omitted unless necessary.

The total elastic distortion of the material can be computed as $\mathbf{F}_e = \mathbf{F}\mathbf{P}$, accounting for the total deformation from the archetype to the current configuration. Within this framework, the first Piola–Kirchhoff stress tensor reads

$$\mathbf{S} = \frac{\partial \psi}{\partial \mathbf{F}} - p\mathbf{F}^{-T} = \frac{1}{\det \mathbf{P}} \frac{\partial \psi_r}{\partial \mathbf{F}_e} \mathbf{P}^T - p\mathbf{F}^{-T}. \quad (9)$$

During the process of deposition of the new cells on the boundary at X_t, the stress state of the newly deposed material must satisfy the boundary condition (8). Specifically, we take

$$\mathbf{T}(\mathbf{x}_t, \mathbf{F}) = \gamma \mathcal{K} n \otimes n, \quad (10)$$

where $\mathbf{x}_t = \boldsymbol{\varphi}_t(X_t)$.[1] Finally, provided that the density of the added point is ρ_0, i.e. the same as the archetype, we get [42]

$$\det \mathbf{P} = 1. \quad (11)$$

In order to find the explicit expression of the transplant, we observe that before cutting the spheroid has a spherical shape. Therefore, we can assume that $\mathbf{P}$ is a function of the radial coordinate only, with

$$\mathbf{P}(R) = P_{RR}(R)e_R \otimes e_R + P_{\Theta\Theta}(R)(\mathbf{I} - e_R \otimes e_R),$$

where P_{RR} and $P_{\Theta\Theta}$ are (unknown) components of the transplant map to be determined. From (11), we immediately get $P_{\Theta\Theta} = P_{RR}^{-1/2}$. We observe that $\boldsymbol{\varphi}_t(X) = X$ is a solution of (6). Indeed, the incompressibility constraint $\det \mathbf{F} = 1$ is satisfied and the first Piola–Kirchhoff stress tensor coincides with the Cauchy stress. By taking $\mathbf{F} = \mathbf{I}$ in (9) we get

$$\mathbf{S} = \mathbf{T} = \mu \mathbf{P}\mathbf{P}^T - p\mathbf{I} \quad (12)$$

By substituting (12) into (10) and observing that $\mathcal{K} = -2/R_t$, after a few passages we are left with the following third-order equation

$$\mu \left(P_{RR}^3(R_t) - 1 \right) R_t + 2\gamma P_{RR}(R_t) = 0. \quad (13)$$

The only positive real solution of such an equation is given by $P_{RR}(R_t) = F(R_t)$, where

$$F(R_t) = \frac{\sqrt[3]{2} \left(G(R_t) \right)^{2/3} - 4\sqrt[3]{3}\ell_c R_t}{6^{2/3} R_t \sqrt[3]{G(R_t)}},$$

$$G(R_t) = \sqrt{96\ell_c^3 R_t^3 + 81R_t^6} + 9R_t^3,$$

where ℓ_c is the elastocapillary length, defined as

$$\ell_{\mathrm{c}} = \frac{\gamma}{\mu}. \quad (14)$$

Summarizing, at $t = T$ we have

$$P_{RR}(R) = \begin{cases} F(R) & \text{it } R \geq R_0, \\ 1 & \text{if } R < R_0. \end{cases}$$

Finally, the balance equation (6) is always satisfied thanks to the pressure variable p. Specifically, under spherical symmetry conditions (6) reduces to

$$\frac{\mathrm{d}S_{rR}}{\mathrm{d}R} + \frac{2(S_{rR} - S_{\theta\Theta})}{R} = 0. \quad (15)$$

---

[1] According to Zurlo and Truskinovsky [39], at the time of the deposition

$$\mathbf{T}(t, \mathbf{x}_t, \mathbf{F}) = \mathbf{T}_p + \mathbf{T}_e,$$

where $\mathbf{T}_p$ is exactly the right-hand side of (10) and satisfies the boundary conditions, while $\mathbf{T}_e$ is a given tensor field accounting for the stress state in other directions, i.e. with $\mathbf{T}_e n = 0$. In the following we assume that there is no force other than the action of the boundary condition (8), and we take $\mathbf{T}_e = \mathbf{0}$.
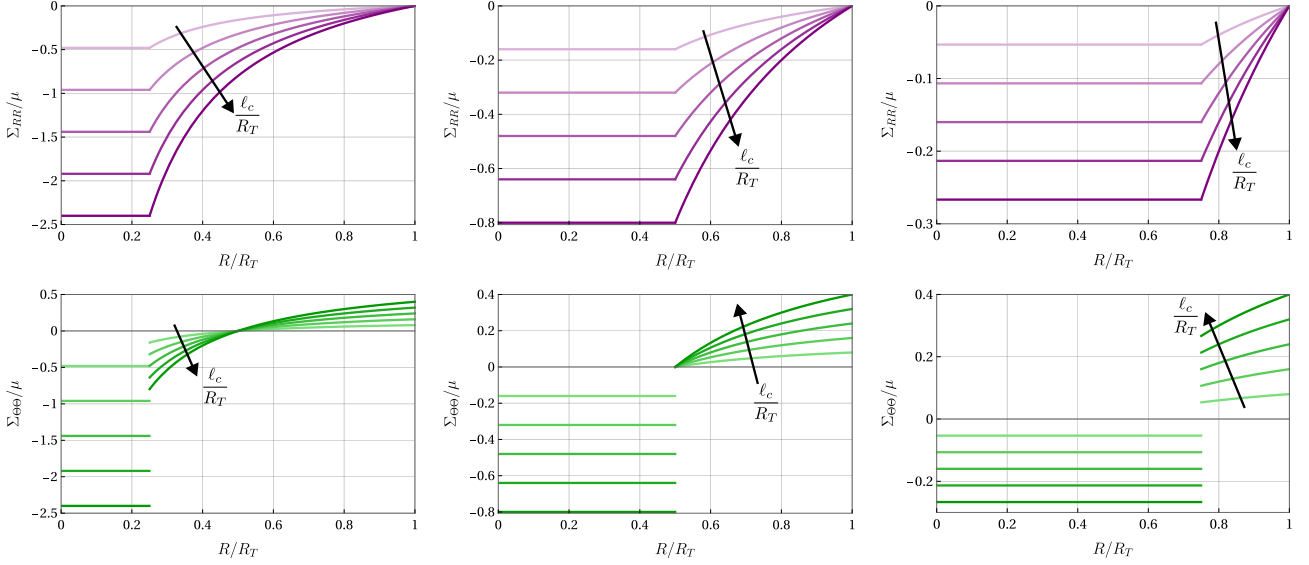
Figure 3: *Plots of dimensionless radial (top) and hoop (bottom) residual stresses, normalized by the shear modulus μ, as a function of the radial position R/R_T. The panels correspond to R_0/R_T values of 0.25 (left), 0.5 (centre), and 0.75 (right). Each curve represents different values of the normalized capillary length $\ell_c/R_T = 0.04, 0.08, \ldots, 0.2$, where $\ell_c = \gamma/\mu$. The direction of increasing ℓ_c/R_T is indicated by arrows, with darker curves representing higher values of ℓ_c/R_T.*

By substitution of (12) in (15), we can integrate with respect to the radial coordinate from R_t to R. Recalling the boundary condition (8), we get

$$p(t, R) = \begin{cases} \mu P_{RR}(R)^2 + 2\gamma \left(\dfrac{2}{R} - \dfrac{1}{R_t} \right) & \text{if } R \geq R_0, \\[2mm] \mu \left(1 - P_{RR}(R_0)^2 \right) + p(t, R_0) & \text{if } R < R_0. \end{cases}$$

The distribution of the transplant map is spatially inhomogeneous. This can give rise to a stress state even if the surface tension is removed at the outer boundary *after the growth of the spheroid*. Such a stress state is called *residual stress*, and it is due by the geometrical incompatibilities induced by surface growth [39], similarly to what happens with volumetric growth [16, 18].

Since there is no deformation induced by surface tension, the residual stress tensor $\boldsymbol{\Sigma}$ can be simply computed as

$$\boldsymbol{\Sigma} = \mu \mathbf{P}\mathbf{P}^T - p_{\boldsymbol{\Sigma}},$$

where $p_{\boldsymbol{\Sigma}}$ is the pressure field in the absence of surface tension. From the boundary condition $\boldsymbol{\Sigma}N = 0$ we get

$$p_{\boldsymbol{\Sigma}}(R) = p(T, R) + \frac{2\gamma}{R_T}.$$

Therefore, the radial and hoop components of the residual stress read

$$\Sigma_{RR} = \begin{cases} 4\gamma \left(\dfrac{1}{R_T} - \dfrac{1}{R} \right), & \text{if } R \geq R_0, \\[3mm] 4\gamma \left(\dfrac{1}{R_T} - \dfrac{1}{R_0} \right), & \text{if } R < R_0, \end{cases}$$

$$\Sigma_{\Theta\Theta} = \begin{cases} 2\gamma \left(\dfrac{2}{R_T} - \dfrac{1}{R} \right), & \text{if } R \geq R_0, \\[3mm] 4\gamma \left(\dfrac{1}{R_T} - \dfrac{1}{R_0} \right), & \text{if } R < R_0. \end{cases}$$

We observe that the resulting residual stress is independent of the material properties, but its magnitude is proportional to the surface tension γ. Representative residual stress profiles are shown in Fig. 3. From these plots, it is clear that the radial residual stress vanishes at $R = R_T$ (consistent with the boundary conditions for residual stress), remains continuous at $R = R_0$, and is compressive (negative) throughout the spheroid. In contrast, the hoop residual stress is tensile in the outer region, becomes zero at $R = R_T/2$ (if $R_0 < R_T/2$), and is compressive in the inner region. In any case, the magnitude of the hoop residual stress at the boundary is independent on R_0 and depends only on the ratio ℓ_c/R_T. Both the radial and the hoop stress are equal in the centre $R < R_0$, in agreement with several experimental results [30, 43]

Thus, the model returned the desired pattern of residual stress, with a tensile region in the outer rim and a compressive stress state in the inner region. In the next section, we analyse the impact of surface tension and growth on the opening of the spheroid due to a radial cut.

3 Deformation of a radially cut tumour spheroid

In this section, we analyse the deformation of a tumour spheroid following a radial incision. The experiments described by [13] investigate the deformation of both newly formed cellular aggregates and more mature ones, with cuts applied at various stages of growth. Many of these experiments focus on aggregates consisting of approximately 5000 cancer cells, which initially exhibit a shape closer to a cylinder rather than a sphere. Importantly, the observed opening in newly formed spheroids upon cutting cannot be attributed to spatially inhomogeneous growth. As discussed previously, this conclusion is supported by experimental evidence showing that only a thin layer of cells at the boundary undergoes circumferential stretch after two days [30].

We begin by presenting a simplified two-dimensional model to describe the cutting of a recently formed tumour spheroid, without considering surface growth. After this, we extend the analysis to a fully three-dimensional model that incorporates growth for spheroids that have been allowed to develop for several days.

3.1 A two-dimensional model of early-stage spheroid cutting

Our goal is to understand the effects of a radial incision on early-stage tumour spheroids. Differently from Sec. 2, we first consider a reference configuration where the spheroid is approximated as a cylinder, which is cut radially, with the cylinder's axis aligned along the Z-axis. To simplify the analysis, we assume that deformations along the Z-axis are negligible, allowing us to focus solely on deformations in the plane perpendicular to the axis.

To model the impact of a radial cut with zero thickness—where no material is removed and a sharp interface is created—we further simplify the problem by analysing only half of the cross-section, assuming axial symmetry throughout.

More specifically, let $\mathcal{S}_0$ be half of the section of the cylinder section lying on the XY plane

$$\mathcal{S}_0 = \{(R\cos\Theta, R\sin\Theta) \in \mathbb{R}^2\},$$

with $0 < R < R_0$ and $0 < \Theta < \pi$. We assume that the portion of the boundary subject to surface tension Σ_γ is given

$$\Sigma_\gamma = \{\boldsymbol{X} = (X, Y) \mid Y = 0 \cap X > R_0 - L \text{ or } |\boldsymbol{X}| = R_0\},$$

where $0 < L < 2R_0$ is the length of the incision.

We apply symmetry boundary condition on the boundary $\Sigma_s = \{\boldsymbol{X} = (X, Y) \mid Y = 0 \cap X < R_0 - L\}$, namely

$$\begin{cases} \boldsymbol{u} \cdot \boldsymbol{e}_Y = 0, \\ \boldsymbol{S}\boldsymbol{e}_Y \cdot \boldsymbol{e}_X = 0. \end{cases} \quad (16)$$

Finally, in order to avoid rigid displacements of the half-disk, we set

$$\boldsymbol{\varphi}(0,0) = \boldsymbol{0}. \quad (17)$$

In the following, we provide an analytical estimate of the opening length induced by surface tension, using a simplified kinematic model.

Analytical estimate using simplified kinematics We now show that, by restricting the set of the admissible deformation fields, we are able to provide an analytical estimate of the opening length of a disk subject to a cut of length $L = R_0$. The polar coordinates in the current configuration are (r, θ)

We restrict the kinematics to a specific set of deformations: we assume that the actual polar coordinates are given by [44, 45]

$$\begin{cases} r = \dfrac{R}{\sqrt{\alpha}}, \\ \theta = \alpha\Theta + (1 - \alpha)\pi, \end{cases} \quad (18)$$

where $\alpha \in (0, 1]$ is a parameter describing the tumour opening, with $\alpha = 1$ corresponding to the undeformed tumour and the tumour opening increasing as α decreases.

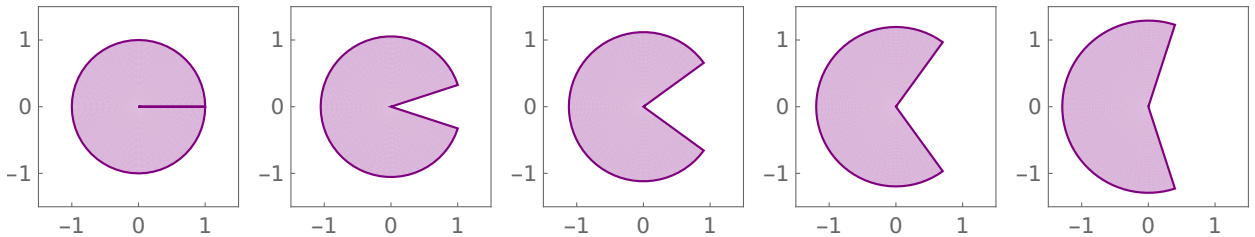The transformations introduced in (18) describe the deformation of a half-disk into a disk sector of

Figure 4: *Representation of the "Pac-Man" deformation described by (18) for $\alpha = 1, 0.9, \ldots, 0.6$ from left to right. All the lengths are rescaled with respect to the initial radius R_0. The deformation is applied to the whole disk for the sake of clarity.*

the same area. By applying this deformation symmetrically to the entire disk, we obtain a "Pac-Man"-like shape, as shown in Fig. 4.

The admissible deformation φ_α defined in (18) is quite restrictive, but it provides enough freedom for the system to release surface energy through elastic deformation, neglecting the rounding of the corners induced by surface tension [46]. We observe that for the admissible deformations

$$\nabla\varphi_\alpha = \frac{\mathrm{d}r}{\mathrm{d}R}e_r \otimes e_R + \frac{r}{R}\frac{\mathrm{d}\theta}{\mathrm{d}\Theta}e_\theta \otimes e_\Theta =$$
$$= \frac{1}{\sqrt{\alpha}}e_r \otimes e_R + \sqrt{\alpha}e_\theta \otimes e_\Theta, \quad (19)$$

so that the deformation gradient has constant coefficients using a polar vector basis.

Thanks to (19), the elastic energy stored in the body (1) can be written as

$$\mathcal{E}_{\mathrm{el}}[\varphi_\alpha] = \frac{\pi\mu R_0^2}{4}\left(\alpha + \frac{1}{\alpha}\right); \quad (20)$$

while the surface energy is given by

$$\mathcal{E}_{\mathrm{s}}[\varphi_\alpha] = \gamma R_0 \left(\frac{1}{\sqrt{\alpha}} + \pi\sqrt{\alpha}\right). \quad (21)$$

In view of (20) and (21), the total energy (3) becomes

$$\mathcal{E}[\varphi_\alpha] = \frac{\pi\mu R_0^2}{4}\left(\alpha + \frac{1}{\alpha}\right) + \gamma R_0 \left(\frac{1}{\sqrt{\alpha}} + \pi\sqrt{\alpha}\right).$$

The energy minima are stationary points of the functional, i.e.

$$\frac{\mathrm{d}}{\mathrm{d}\alpha}\mathcal{E}[\varphi_\alpha] = 0. \quad (22)$$

By solving (22), we get

$$\frac{\ell_c}{R_0} = \frac{\pi\left(1 - \alpha^2\right)}{2\sqrt{\alpha}(\pi\alpha - 1)}. \quad (23)$$

The expression given by (23) can be inverted numerically to find α. Given the opening angle, it is possible to compute the opening length ω of the cut cylinder as

$$\omega = 2u(0, R_0) \cdot e_X = \frac{2R_0 \sin\alpha}{\sqrt{\alpha}}. \quad (24)$$

A plot of the opening predicted by this single-degree-of-freedom model is reported in Fig. 5, where we observe an almost linear relation between ω and the elastocapillary length ℓ_c.

Of course, this is a very simplified model, where the energy depends only on a single scalar variable, that is α. We are restricted to considering just a cut length equal to the radius and other effects. Moreover, the deformation close to sharp corners induced by surface tension is neglected [46, 47]. In the following, we compare the proposed approximation by with numerical simulations.

Finite element approximation The problem of spheroid cutting cannot be solved analytically if we allow non-homogeneous deformations. Therefore, we have to rely on numerical simulations. In what follows, we adopt the finite element method. Specifically, the problem can be written in weak form as

Find (u, p) such that, for all (v, q) :

$$\int_\mathcal{S} \mathbf{S} : \nabla v \,\mathrm{d}V - \int_{\Sigma_\gamma} \gamma\mathcal{K}v \cdot \mathbf{F}^{-T}N \,\mathrm{d}S + \quad (25)$$
$$- \int_\mathcal{S} q(\det \mathbf{F} - 1) \,\mathrm{d}V = 0,$$

where (v, q) are the test functions. Both (u, p) and (v, q) must belong to an appropriate functional space ensuring that the boundary conditions (16) and (17) are satisfied. We do not enter into the mathematical details, we refer to [48, 49] for a detailed discussion.

The half-disk domain, $\mathcal{S}$, is discretized using a triangular mesh. Since surface tension induces singular stresses near sharp angles [46], the mesh is refined around the vertices of the cut to improve the accuracy of the numerical solution. We employ a mixed formulation with Taylor-Hood elements, discretizing the displacement and pressure fields using piecewise quadratic and linear functions, respectively. This choice ensures the well-posedness of the discrete problem and prevents the emergence of spurious pressure modes [50].

The implementation is carried out using the FEniCS library. Surface tension is incrementally increased by a step size $\Delta\gamma$. The problem (25) is solved using Newton's method, with the solution from $\gamma = \gamma_k$ serving as the initial guess for the subsequent Newton iteration at $\gamma = \gamma_{k+1} = \gamma_k + \Delta\gamma$. The increment
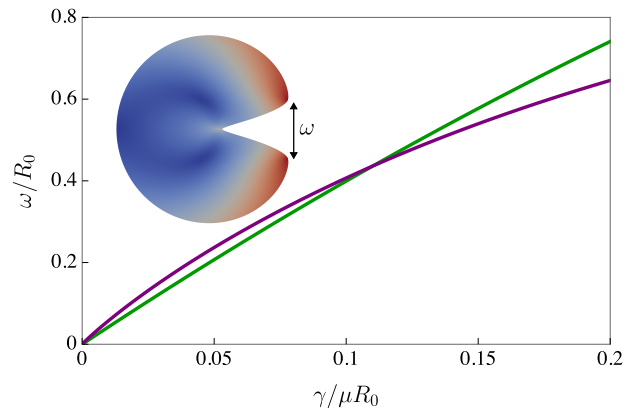

Figure 5: *Opening length ω as a function of the surface tension γ for a radial cut of length R_0 of a disk. The purple curve denote the numerical prediction, while the green curve is the result of the single-degree-of-freedom model of Eqs. (23)-(24). All the quantities are non-dimensionalised with respect to the radius R_0 and the shear modulus μ.*
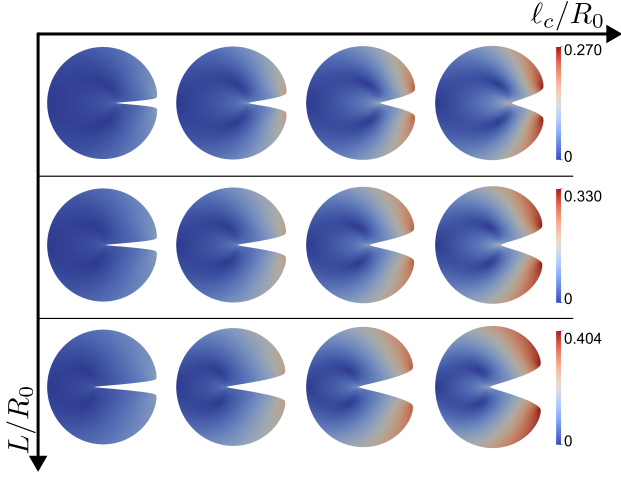
Figure 6: *Morphological diagram showing the current configuration of the 2D model of the cut spheroid for $\ell_c/R_0 = 0.05, 0.1, 0.15, 0.2$ and $L/R_0 = 0.8, 1, 1.2$. The colour bar denotes the norm of the displacement $\boldsymbol{u}$ non-dimensionalised with respect to R_0.*
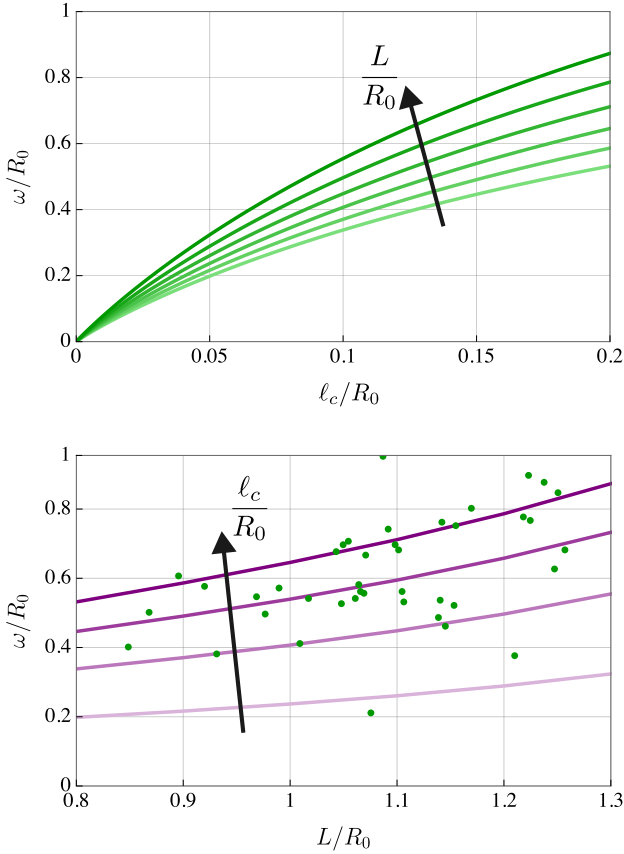

Figure 7: *Plot of the opening ω of the cut disk as a function of the elastocapillary length (top) and of the incision length (bottom). All lengths are non-dimensionalised with respect to R_0. The value of L/R_0 in the top panel are $0.8, 0.9, \ldots, 1.3$, while the values of ℓ_c/R_0 in the bottom panel are $0.05, 0.1, 0.15, 0.2$. In the bottom panel we also show the experimental data for a spheroid with 5000 cells at the beginning of the experiment and cut after two days.*

$\Delta\gamma$ is automatically adjusted if the Newton method fails to converge or converges in fewer than three iterations. This algorithm is implemented using the library BiFEniCS [51].

Results of the two-dimensional simulations In Fig. 5, we compare the theoretical predictions of the single-degree-of-freedom analytical model given by (23)-(24) with the outcomes of the numerical simulations (with an incision length of $L = R_0$).

We observe that for moderate values of the dimensionless parameter ℓ_c/R_o there is a very good agreement between the analytical and the numerical model. When $\ell_c/R_0 > 1.5$ the discrepancy between the two models starts to be more relevant. This can be due to the non-homogeneity of the deformations close to the corners, which is particularly evident for large values of ℓ_c/R_0. In Fig. 6, we present the current configurations of the cut sphere for various values of the incision length L and of the ratio ℓ_c/R_0. A quantitative plot of the different opening length observed as we change the parameters of the model is proposed in Fig. 7, together with a comparison with the experimental results of Guillaume et al. (see [13]) for a newly created spheroid (i.e. without growth). We observe that surface tension has a strong influence on the opening length (i.e. as we vary $\ell_c/R_0 = \gamma/\mu R_0$). Conversely, the incision depth as a smaller influence on the resulting deformations. From the experimental data, we can estimate that ℓ_c/R_0 is around 0.15, even though there is some variance in the experimental results. Given that the shear modulus is approximately 1 kPa and the radius
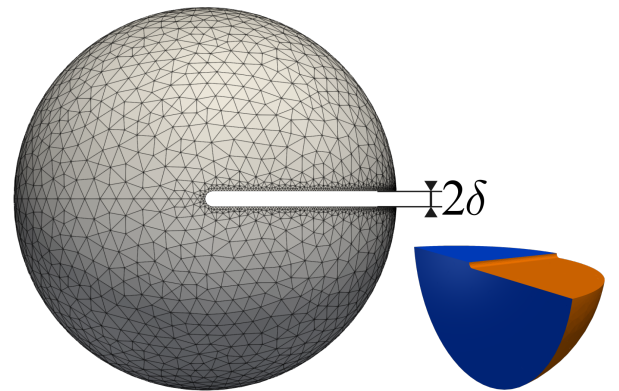

Figure 8: *Representation of the full spheroid, with δ indicating the thickness of the cut. In the numerical simulations, only a quarter of the cut spheroid, as shown in the inset, is modelled. The blue surface in the inset corresponds to the region with symmetry boundary conditions, while the orange surface denotes the free boundary subject to surface tension. The mesh is refined near the cut edges to improve accuracy in these regions.*
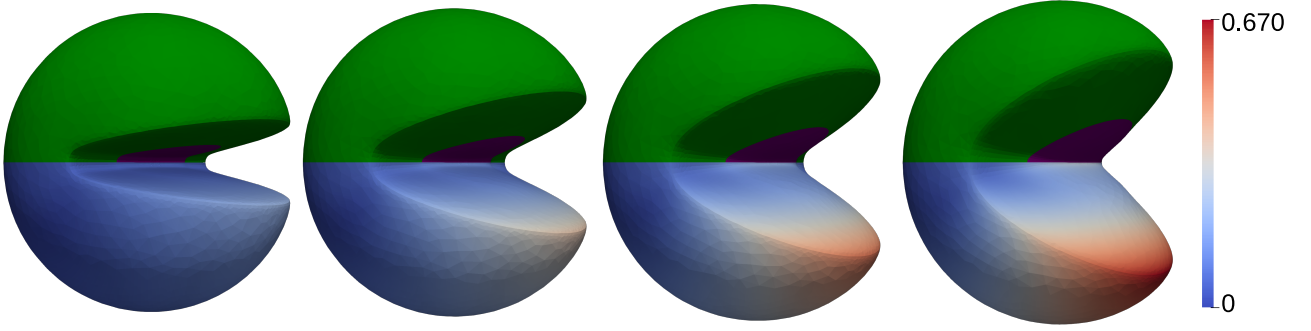
Figure 9: *Current configuration of a cut spheroid after growth, with $R_T = 2R_0$. From left to right, $\ell_c/R_T = 0.05, 0.1, 0.15, 0.2$. The colour-bar denotes $\|\boldsymbol{u}\|/R_T$. On the top half of the spheroid, we denote in purple the initial region occupied by the spheroid at $t = 0$, while the green part indicates the grown region.*

is around $450\,\mu$m [13], the surface tension acting on the spheroid is estimated to be about $68\,\text{mN/m}$.

In the experiments reported in [13], spheroids observed for growth have a reduced initial cell count. This has important consequences for the shape of the spheroid, as it retains a more spherical form. Consequently, we must abandon the assumption of cylindrical symmetry to model spheroid incision after growth, necessitating three-dimensional simulations to replicate these experiments.

3.2 Simulations of three-dimensional spheroid cutting

In the paper [13], the authors provides data on the opening lengths observed after cutting spheroids that had been cultured for six days, reporting a doubling of their initial radius. Therefore, in what follows we focus on the case of $R_T = 2R_0$ in the simulations with growth. These spheroids are characterized by an initial cell count of 500, with a final radius $R_T \sim 450\mu$m at $T = 6$ days.

Implementation The transition from 2D to 3D geometries introduces additional computational challenges. While the weak form remains consistent with that in (25), the issue arises at the cut in the middle of the spheroid. Here, the cut spans the entire line, leading to a blow-up of the stress and pressure fields due to the infinite curvature at the tip of the cut [46, 47]. These singularities induce large deformations near the cut tip, which can create difficulties in the convergence of Newton's algorithm. To address this issue and model the mass depletion during the cutting process, we represent the cut as a crack with a finite thickness 2δ, as illustrated in Fig. 8. Specifically, in the following, we use a value of $0.05R_T$ for δ.

Results of the three-dimensional simulations In Fig. 9, we show the current configuration of a grown spheroid following the cut for different values of ℓ_c/R_T. We observe, as for the two-dimensional simu-
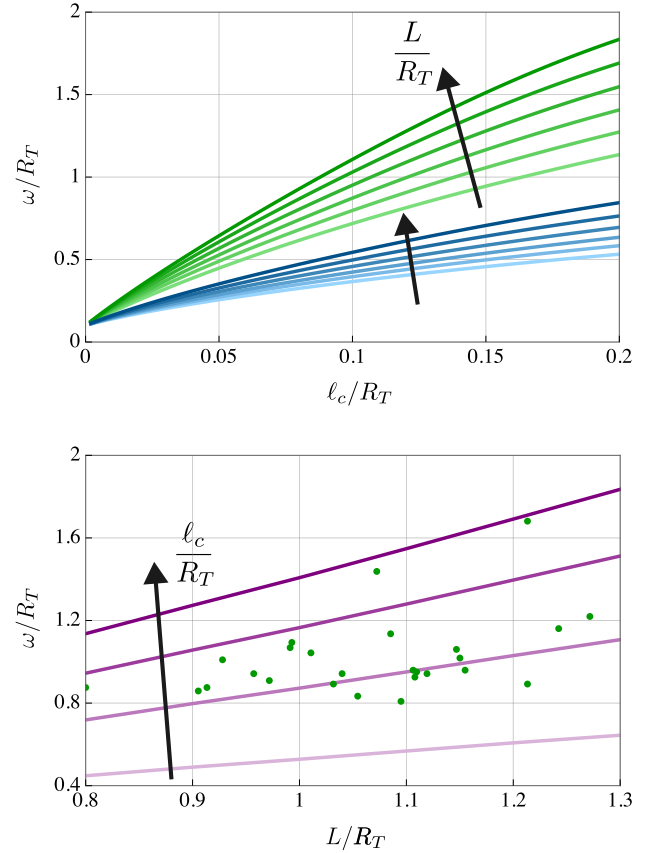

Figure 10: *Plot of the opening ω of the cut sphere as a function of the elastocapillary length (top) and of the incision length (bottom). In the top panel, green curves indicate the opening of a spheroid after growth, in blue we show the results of a cut sphere without growth ($R_0 = R_T$). All lengths are non-dimensionalised with respect to R_T. The value of L/R_T in the top panel are $0.8, 0.9, \ldots, 1.3$, while the values of ℓ_c/R_T in the bottom panel are $0.05, 0.1, 0.15, 0.2$. In the bottom panel we also show the experimental data for a spheroid with 500 cells at the beginning of the experiment and cut after six days, from [13].*

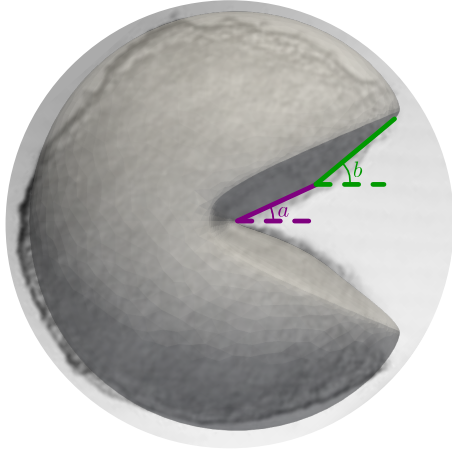lations, an increment in the tumour opening as the surface tension increases. The sharp edges of the cut

Figure 11: *Superposition of the experimental image of a cut spheroid after 6 days of growth (initial number of cells: 500; image adapted from [13]) with a corresponding numerical simulation ($\ell_c/R_T = 0.13$, $L/R_T = 1.1$). The purple lines highlight the opening of the cut in the region already existing at $t = 0$, showing an opening angle of approximately $23°$ (indicated with a in the figure). The green lines represent the opening of the grown region of the spheroid, where the opening angle b increases to around $40°$.*

are rounded by the effect of surface tension [46].

The residual stresses accumulated in the spheroid during surface growth nearly double the tumour's opening compared to simulations without growth, as illustrated in Fig.10 (top). Notably, the simulation results without surface growth (blue lines) are comparable to those shown in Fig.7 for a circular domain, suggesting that the domain geometry plays a minor role in the mechanics of tumour opening post-incision.

A comparison with the experimental measurements of the opening length from Guillaume et al. [13] is shown in Fig. 10 (bottom). We observe a nearly linear relationship between the incision depth and the measured opening, although the slope of the curves is relatively small. This indicates that incision depth plays a minor role in the overall quantitative opening of the tumour. Instead, surface tension seems to have a more dominant influence. From the experimental results, we estimate the elastocapillary length to be between $0.1R_T$ and $0.15R_T$. Given that the shear modulus is approximately $1\,\mathrm{kPa}$ and the radius is around $450\,\mu\mathrm{m}$ [13], the surface tension acting on the spheroid is estimated to be in the range of $45\,\mathrm{mN/m} < \gamma < 68\,\mathrm{mN/m}$. This range closely aligns with the estimates reported by Riccobelli and Bevilacqua [31], who estimated $\gamma \sim 100\,\mathrm{mN/m}$ using a different methodology.

Interestingly, we observe that the residual stress also influences the shape of the cut: in the grown re-

gion, the opening of the tumour is more pronounced, as shown in Fig. 11. This change in the opening is absent if the spheroid is cut just after its creation, see Fig 1 (right). In Fig. 11, we remark that there is a strong agreement between the shape predicted by the numerical simulations and the one observed in the experiments.

4 Discussion and concluding remarks

Despite the large amount of literature on the mechanics of solid tumours, even basic aspects of cell proliferation and solid stress development are poorly understood. The theoretical framework of this paper provides a new perspective on these fundamental issues. As discussed in [31], we argue that surface tension generated by cell-cell adhesion and active contractility plays a crucial role in determining the stress state and guiding cell proliferation in the early stages of tumour growth.

We have focused our attention on solid tumour spheroids, proposing a mathematical model of tumour surface accretion based on the theory of Zurlo and Truskinovsky [39–41]. Surface tension elastically deforms newly produced cells on the free surface, resulting into a compression of the cells along the radial direction. This process generates an inhomogeneous prestretch and a geometrically incompatible relaxed state. The pattern of residual stress predicted by the model resembles that observed in real tumours [1, 8]. The model predicts a structure of the spheroid composed of an inner core subject to isotropic compression and an outer rim where cells are radially compressed and circumferentially elongated, consistently with experimental observations, see Fig. 5 in [43].

To validate our theoretical framework, we have investigated the deformation of spheroids following radial incisions. In [13], different opening length are observed depending on the spheroid's age. Tumour spheroids typically requires two days to self-aggregate [30]. After this period, the bulk of the spheroid shows negligible residual stress. Instead, the primary source of stress within the spheroid can be attributed to the tissue surface tension, resulting in a pressure-like stress state in bulk [30, 31]. We have shown that the radial cut generates an opening of the spheroid driven by surface tension, even in the absence of residual stress. We derived a simplified analytical approximation by means of classical universal solutions of nonlinear elasticity, which provides an estimation of tumour opening. However, this model neglects the non-uniform deformations arising from singular stresses at the cut edges, which are caused

by the infinite curvature of the free surface in the reference configuration.

To overcome these limitations, we have performed finite element simulations. The results of these simulations are reported in Figs. 5-7. We have shown that, despite its simplicity, our analytical approximation is in good agreement with the results of the numerical simulations. We have also included the effect of growth and the related mechanical stress in older spheroids. The results of the simulations for growing spheroids are reported in Figs. 9-11. The morphology predicted by the numerical simulations strikingly matches with the experimental evidences. The numerical simulations in early and grown spheroids are tested with the quantitative data provided by Guillaume et al. [13]. Both cases indicate that the surface tension acting on the spheroids is about $60\,\mathrm{mN/m}$, similarly to previous estimates [31].

The results of this work highlight the key role that surface tension and elasticity play in the growth of solid tumours. The proposed model correctly captures both the proliferation pattern within the tumour and the development of mechanical stress in the early stages of tumour progression. These key features play a crucial role in the subsequent vascularization of the tumour and possible tissue invasion in cancer. Open problems related to this research are correlated with mechano-transduction phenomena in solid tumours. It is well-known that mechanical stress can inhibit growth, and a mathematical framework to include mechanical feedback in volumetric growth law is quite established. Its extension to surface growth is non-trivial. Other problems involve extending the proposed model to compressible constitutive law. Indeed, the poroelastic nature of the spheroid can induce volumetric deformations of the solid matrix, and adding a slight compressibility would improve the model accuracy. The compressibility of the spheroid can induce discrepancies between the reference and the current configurations, leading to a more complex reconstruction of the surface accretion process, as discussed in [41]. In this respect, also a coupled theory between surface and volumetric growth in biological tissues is needed.

Data availability statement The source code and experimental data from [13] are available at `https://github.com/riccobelli/cutting_spheroids`

References

[1] T. Stylianopoulos et al. 'Causes, consequences, and remedies for growth-induced solid stress in murine and human tumors'. *Proc. Natl. Acad. Sci. USA* 109.38 (2012), pp. 15101–15108.

[2] M. Zanoni et al. 'Modeling neoplastic disease with spheroids and organoids'. *J. Hematol. Oncol.* 13.1 (2020).

[3] R. K. Jain, J. D. Martin and T. Stylianopoulos. 'The Role of Mechanical Forces in Tumor Growth and Therapy'. *Annu. Rev. Biomed. Eng.* 16.1 (2014), pp. 321–346.

[4] G. Helmlinger et al. 'Solid stress inhibits the growth of multicellular tumor spheroids'. *Nat. Biotechnol.* 15.8 (1997), pp. 778–783.

[5] F. Montel et al. 'Stress Clamp Experiments on Multicellular Tumor Spheroids'. *Phys. Rev. Lett.* 107.18 (2011).

[6] F. Montel et al. 'Isotropic stress reduces cell proliferation in tumor spheroids'. *New J. Phys.* 14.5 (2012), p. 055008.

[7] P. Mascheroni et al. 'Predicting the growth of glioblastoma multiforme spheroids using a multiphase porous media model'. *Biomech. Model. Mechanobiol.* 15.5 (2016), pp. 1215–1228.

[8] D. Ambrosi et al. 'Solid Tumors Are Poroelastic Solids with a Chemo-mechanical Feedback on Growth'. *J. Elast* 129.1–2 (2017), pp. 107–124.

[9] M. Dolega et al. 'Mechanical behavior of multicellular spheroids under osmotic compression'. *J. Mech. Phys. Solids* 147 (2021), p. 104205.

[10] A. Erlich and P. Recho. 'Mechanical feedback in regulating the size of growing multicellular spheroids'. *J. Mech. Phys. Solids* 178 (2023), p. 105342.

[11] M. Pandey et al. 'Mechanical compression regulates tumor spheroid invasion into a 3D collagen matrix'. *Phys. Biol.* 21.3 (2024), p. 036003.

[12] T. Colin et al. 'Experimental estimation of stored stress within spherical microtissues: What can and cannot be inferred from cutting experiments'. *J. Math. Biol.* 77.4 (2018), pp. 1073–1092.

[13] L. Guillaume et al. 'Characterization of the physical properties of tumor-derived spheroids reveals critical insights for pre-clinical studies'. *Sci. Rep.* 9.1 (2019).

[14] N. V. Kosheleva et al. 'Building a tissue: Mesenchymal and epithelial cell spheroids mechanical properties at micro- and nanoscale'. *Acta Biomater.* 165 (2023), pp. 140–152.

[15] A. P. Browning et al. 'Quantitative analysis of tumour spheroid structure'. *eLife* 10 (2021).

[16] E. K. Rodriguez, A. Hoger and A. D. McCulloch. 'Stress-dependent finite growth in soft elastic tissues'. *J. Biomech.* 27.4 (1994), pp. 455–467.

[17] A. Goriely and M. B. Amar. 'On the definition and modeling of incremental, cumulative, and continuous growth laws in morphoelasticity'. *Biomech. Model. Mechanobiol.* 6.5 (2006), pp. 289–296.

[18] A. Goriely. *The mathematics and mechanics of biological growth*. Vol. 45. Springer, 2017.

[19] L. A. Taber. 'Biomechanics of Growth, Remodeling, and Morphogenesis'. *Appl. Mech. Rev.* 48.8 (1995), pp. 487–545.

[20] L. A. Taber and R. Perucchio. 'Modeling heart development'. *J. Elast.* 61 (2000), pp. 165–197.

[21] V. Balbi and P. Ciarletta. 'Morpho-elasticity of intestinal villi'. *J. R. Soc. Interface* 10.82 (2013), p. 20130109.

[22] M. Ben Amar and F. Jia. 'Anisotropic growth shapes intestinal tissues during embryogenesis'. *Proc. Natl. Acad. Sci. USA* 110.26 (2013), pp. 10525–10530.

[23] C. J. Chuong and Y. C. Fung. 'Residual Stress in Arteries'. In: *Frontiers in Biomechanics*. Springer New York, 1986, pp. 117–129.

[24] G. A. Holzapfel and R. W. Ogden. 'Modelling the layer-specific three-dimensional residual stresses in arteries, with an application to the human aorta'. *J. R. Soc. Interface* 7.46 (2009), pp. 787–799.

[25] R. Araujo and D. McElwain. 'New insights into vascular collapse and growth dynamics in solid tumors'. *J. Theor. Biol.* 228.3 (2004), pp. 335–346.

[26] J. MacLaurin et al. 'The buckling of capillaries in solid tumours'. *Proc. R. Soc. A* 468.2148 (2012), pp. 4123–4145.

[27] D. Riccobelli and P. Ciarletta. 'Morpho-elastic model of the tortuous tumour vessels'. *Int. J. Non-Linear Mech.* 107 (2018), pp. 1–9.

[28] B. J. Walker et al. 'Minimal Morphoelastic Models of Solid Tumour Spheroids: A Tutorial'. *Bull. Math. Biol.* 85.5 (2023).

[29] M. Delarue et al. 'Mechanical Control of Cell flow in Multicellular Spheroids'. *Phys. Rev. Lett.* 110.13 (2013).

[30] W. Lee et al. 'Dispersible hydrogel force sensors reveal patterns of solid mechanical stress in multicellular spheroid cultures'. *Nat. Commun.* 10.1 (2019).

[31] D. Riccobelli and G. Bevilacqua. 'Surface tension controls the onset of gyrification in brain organoids'. *J. Mech. Phys. Solids* 134 (2020), p. 103745.

[32] M. L. Manning et al. 'Coaction of intercellular adhesion and cortical tension specifies tissue surface tension'. *Proc. Natl. Acad. Sci. USA* 107.28 (2010), pp. 12517–12522.

[33] I. Ang et al. 'Elastocapillary effects determine early matrix deformation by glioblastoma cell spheroids'. *APL Bioeng.* 8.2 (2024).

[34] R. Skalak et al. 'Analytical description of growth'. *J. Theor. Biol.* 94.3 (1982), pp. 555–577.

[35] A. DiCarlo. 'Surface and bulk growth unified'. In: *Mechanics of Material Forces*. Springer, 2005, pp. 53–64.

[36] P. Ciarletta, L. Preziosi and G. Maugin. 'Mechanobiology of interfacial growth'. *J. Mech. Phys. Solids* 61.3 (2013), pp. 852–872.

[37] F. Sozio and A. Yavari. 'Nonlinear mechanics of surface growth for cylindrical and spherical elastic bodies'. *J. Mech. Phys. Solids* 98 (2017), pp. 12–48.

[38] V. von Streng et al. 'Morphogenesis and proportionate growth: A finite element investigation of surface growth with coupled diffusion'. *J. Mech. Phys. Solids* 146 (2021), p. 104211.

[39] G. Zurlo and L. Truskinovsky. 'Printing Non-Euclidean Solids'. *Phys. Rev. Lett.* 119.4 (2017).

[40] G. Zurlo and L. Truskinovsky. 'Inelastic surface growth'. *Mech. Res. Commun.* 93 (2018), pp. 174–179.

[41] L. Truskinovsky and G. Zurlo. 'Nonlinear elasticity of incompatible surface growth'. *Phys. Rev. E* 99.5 (2019).

[42] M. Epstein. *The Elements of Continuum Biomechanics*. Wiley, 2012.

[43] M. E. Dolega et al. 'Cell-like pressure sensors reveal increase of mechanical stress towards the core of multicellular spheroids under compression'. *Nat. Commun.* 8.1 (2017).

[44] M. Singh and A. C. Pipkin. 'Note on Ericksen's problem'. *Z. Angew. Math. Phys.* 16.5 (1965), pp. 706–709.

[45] S. A. Silling. 'Creasing Singularities in Compressible Elastic Materials'. *J. Appl. Mech.* 58.1 (1991), pp. 70–74.

[46] S. Mora and Y. Pomeau. 'Softening of edges of solids by surface tension'. *J. Phys. Condens. Matter* 27.19 (2015), p. 194112.

[47] S. Mora et al. 'Solid Drops: Large Capillary Deformations of Immersed Elastic Rods'. *Phys. Rev. Lett.* 111.11 (2013).

[48] J. Bonet and R. D. Wood. *Nonlinear Continuum Mechanics for Finite Element Analysis*. Cambridge University Press, 2008.

[49] A. Quarteroni. *Numerical Models for Differential Problems*. Springer Milan, 2014.

[50] D. Boffi, F. Brezzi and M. Fortin. *Mixed Finite Element Methods and Applications*. Springer Berlin Heidelberg, 2013.

[51] D. Riccobelli, G. Noselli and A. DeSimone. 'Rods coiling about a rigid constraint: helices and perversions'. *Proc. R. Soc. A* 477.2246 (2021), p. 20200817.